Wrinkling Dynamics of Fluctuating Vesicles in Time-dependent Viscous Flow: Supplementary Material

Kai Liu, Caleb Hamilton, Jun Allard, John Lowengrub, Shuwang Li

April 13, 2016

Contents

SM.1 Nondimensionalization

Let $R=\sqrt{A/\pi}$ be the effective vesicle radius (A is the total area of the vesicle) and L be the total arclength. Let S be the strength of the applied extensional flow. Then, nondimensionalizing time by $t'=St$ and space by $\mathbf{x}'=\mathbf{x}/\mathbf{R}$, the nondimensional stochastic, immersed boundary equations can be written as:

$$Re\ \partial\mathbf{u}'/\partial t' = \nabla'^2\mathbf{u}'-\nabla'\tilde{p}'+\chi^{-1}\Lambda'(\mathbf{F}'_{\mathbf{X}'})+\chi^{-1/2}\ Ku_B\ \mathscr{C}^{1/2}\nabla'\cdot\mathbf{W}', \tag{SM.1}$$

$$\nabla'\cdot\mathbf{u}' = 0, \tag{SM.2}$$

$$\nabla'_s\cdot\Upsilon'(\mathbf{u}') = 0, \tag{SM.3}$$

$$\Lambda'(\mathbf{F}'_{\mathbf{X}}) = \int_{\mathscr{S}(t')'}\mathbf{F}'_{\mathbf{X}}(t')\ \delta'_{a'}(\mathbf{x}'-\mathbf{X}'(s',t'))\ ds', \tag{SM.4}$$

$$\Upsilon'(\mathbf{u}') = \int_{\mathscr{D}'}\mathbf{u}'(\mathbf{x}',t')\ \delta'_{a'}(\mathbf{x}'-\mathbf{X}'(s',t'))\ d\mathbf{x}', \tag{SM.5}$$

$$d\mathbf{X}'/dt' = \Upsilon'(\mathbf{u}'), \tag{SM.6}$$

where $Re=S\rho R^2/\eta$ is the Reynolds number, $\chi=S\eta R^3/\kappa$ is the nondimensional strain, $Ku_B=\sqrt{k_BT/\kappa}$ is a bending Kubo number[1,2], and $\mathscr{C}=R/L_d$ is a confinement number. The nondimensional velocity $\mathbf{u}'=\mathbf{u}/(SR)$, $p'=(p-\Lambda k_BT)/(\eta S)$ is a modified nondimensional pressure that incorporates the drift term. The nondimensional force $\mathbf{F}'_{\mathbf{X}'}$ is given by

$$\mathbf{F}'_{\mathbf{X}'}=\left(\frac{\partial^2H'}{\partial s'^2}+\frac{1}{2}H'^3-H'\sigma'\right)\mathbf{n}+\frac{\partial\tilde{\sigma}'}{\partial s'}\mathbf{t}, \tag{SM.7}$$

where $s'=s/R$ is the nondimensional arclength, $H'=RH$, and $\sigma'=\left(\sigma R^2\right)/\kappa$ is a nondimensional elastic tension. Finally, $\delta'_{a'}=R^2\delta_{a/R}$ is the nondimensional two-dimensional approximate delta function, and the nondimensional white noise tensor $\mathbf{W}'$ satisfies

$$\mathbf{E}\left(W'_{ij}(\mathbf{x}',t')W'_{kl}(\mathbf{y}',\tau')\right)=\delta_{ik}\delta_{jl}\delta'_{\mathbf{x}'}(\mathbf{x}'-\mathbf{y}')\delta'_{t'}(t'-\tau'), \tag{SM.8}$$

where $\delta'_{t'}=S^{-1}\delta_{St}$ and $\delta'_{\mathbf{x}'}=R^2\delta_{\mathbf{x}/R}$ are nondimensional temporal and spatial delta functions.

SM.2 Wrinkling dynamics of a nearly circular vesicle: Perturbation theory

The stochastic partial differential equations governing the motion of a nearly circular vesicle in Stokes flow can be simplified to a system of stochastic ordinary differential equations using perturbation theory. Here, we outline this procedure and focus on the model for thermal fluctuations. We assume that the vesicle interface $r_\Gamma=R(1+P)$ is a perturbed circle of radius R, where the perturbation P can be written as the Fourier series:

$$P(t,\phi)=\sum_m P_m(t)\exp(im\phi)/\sqrt{2\pi}, \tag{SM.9}$$

where P_m are the Fourier coefficients. In the deterministic case, following[3–5], the Stokes equations and boundary conditions are solved in the perturbed domain to first order in P to obtain an evolution equation for the Fourier coefficients of P:

$$\frac{dP_m}{dt}=S\ \mathrm{sgn}(t_{rev}-t)(\delta_{m,2}+\delta_{m,-2})-\frac{\kappa}{\eta R^3}\beta_mE_mP_m, \tag{SM.10}$$

where $\mathrm{sgn}(t)$ is the sign of t. Here, $E_m=(m^2-1)(m^2-3/2+\sigma)$ is the elasticity coefficient, $\beta_m=\frac{|m|}{4(m^2-1)}$ is the mobility coefficient, and σ is the elastic tension. The elastic tension σ at each instant is determined such that the global constraint $d\left(\Sigma(m^2-1)|P_m|^2\right)/dt=0$ is fulfilled. This gives

$$\sigma=\left(6S\ \mathrm{sgn}(t_{rev}-t)\mathrm{Re}(P_2)-\bar{\Gamma}+\bar{\zeta}\right)/\bar{A}, \tag{SM.11}$$

where $\bar{\Gamma} = \frac{\kappa}{\eta R^3}\sum(m^2-1)\Gamma_m|P_m|^2$, $\bar{A} = \frac{\kappa}{\eta R^3}\sum(m^2-1)A_m|P_m|^2$, $\bar{\zeta} = \sum(m^2-1)P_m^*\zeta_m$, and $\Gamma_m = |m|(m^2-3/2)/4$, $A_m = |m|/4$. A detailed derivation can be found in [3,4].

At nonzero temperatures, thermal fluctuations can be modeled as an additive noise term in Eq. (SM.10) following [3,6,7]. This yields the stochastic differential equation

$$\frac{dP_m}{dt} = S\ \mathrm{sgn}(t_{rev}-t)(\delta_{m,2}+\delta_{m,-2}) - \frac{\kappa}{\eta R^3}\beta_m E_m P_m + \zeta_m, \quad \text{(SM.12)}$$

where ζ_m describes the contribution of thermal fluctuations, which needs to be modeled. We assume that (i) $S=0$, (ii) the elastic tension σ is constant, (iii) the vesicle is in equilibrium, and (iii) ζ_m is a complex-valued white noise random variable that is independent of P_m. In particular, we take

$$\zeta_{\pm m}(t) = \Xi_m \frac{dB_m}{dt}(t), \ \text{ for } m = 1,2,3,..., \ t \geq 0, \quad \text{(SM.13)}$$

where $B_m(t)$ are independent complex-valued Weiner processes (e.g., standard complex Brownian motion) and Ξ_m are scaling factors whose values we derive below.

Consider the deviation of the m^{th} perturbation P_m from its mean

$$\delta P_m = P_m - \langle P_m \rangle, \quad \text{(SM.14)}$$

where $\langle\cdot\rangle$ denotes the mean value. Then, the solution to Eq. (SM.12) with $S=0$ then reads as

$$\delta P_m(t) = \delta P_m(0) e^{-\left(\kappa/\eta_2 R^3\right)\beta_m E_m t} + \Xi_m \int_0^t e^{\left(\kappa/\eta_2 R^3\right)\beta_m E_m (u-t)} dB_m(u), \quad \text{(SM.15)}$$

where the integrals are Itô integrals and $\delta P_m(0)$ is the initial value. By Itô's Isometry, we obtain

$$\mathbf{E}\left(\left|\delta P_m(t) - \delta P_m(0) e^{-\left(\kappa/\eta_2 R^3\right)\beta_m E_m t}\right|^2\right) = \Xi_m^2 \int_0^t e^{2\left(\kappa/\eta_2 R^3\right)\beta_m E_m (u-t)} du, \quad \text{(SM.16)}$$

where $\mathbf{E}$ denotes the expectation.

Following the Einstein relation, we set the average energy of each mode to be proportional to $k_B T$. Here, the relevant energy is the elastic energy, which in two-dimensions, can be written as

$$E_\kappa = \frac{\kappa}{2R}\sum_{m\neq 0} E_m |P_m|^2, \quad \text{(SM.17)}$$

up to quadratic order in P. Because we are in two-dimensions, we again need to scale $k_B T$ by a length scale L_d as in Sec. 2.2 in the main text. Thus, the fluctuation-dissipation theorem gives

$$\frac{\kappa}{2R} E_m \left\langle |P_m|^2 \right\rangle = \frac{1}{2L_d} k_B T. \quad \text{(SM.18)}$$

Because $\langle P_m \rangle = 0$ as $t \to \infty$, we obtain from Eqs. (SM.16) and (SM.18) that

$$\Xi_m^2 = \frac{2\beta_m k_B T}{\eta R^2 L_d}, \quad \text{(SM.19)}$$

which gives the correlations:

$$\langle \zeta_m(t)\zeta_n(\tau)\rangle = \frac{2\beta_m k_B T}{\eta R^2 L_d}\delta_{m,-n}\delta(t-\tau). \quad \text{(SM.20)}$$

Note that the factor L_d in Eq. (SM.20) was replaced by R in the 2D analysis presented by Finken et al.[3], which would be the corresponding scaling in three dimensions. Here, we take the value of L_d used in the fully nonlinear simulations. Since $R < L_d$, this means that the thermal fluctuations are smaller than would be the case if R was used instead as in [3], although the results using the two choices are qualitatively similar.

Finally, assuming that Eq. (SM.20) is also valid for the vesicle in a non-vanishing extensional flow, we can then investigate the stochastic wrinkling dynamics by solving Eq. (SM.12) numerically for a finite number of modes. Here, we took $0 < |m| \leq 256$ and used a second-order stochastic Runge-Kutta (RK2) method [8] to perform the time integration. The initial data for the perturbation theory is obtained from taking the Fourier coefficients of the vesicle shape just before the flow is reversed.

SM.3 Numerical method

We use a finite difference scheme to discretize the fluid equations. The membrane is represented by N nodes that are connected by springs each with spring constant λ_L. We write the velocity $\mathbf{u} = \mathbf{u}_p + \mathbf{u}_\infty$ where $\mathbf{u}_p$ is a doubly-periodic function and $\mathbf{u}_\infty = S\ \mathrm{sgn}(t_{rev}-t)(y,-x)$ is the applied extensional flow. The discretized system is given by

$$\rho(\mathbf{u}_p^{n+1}-\mathbf{u}_p^n)/\Delta t = \eta L\mathbf{u}_p^{n+1} - \mathbf{D}\tilde{p}^{n+1} + \Lambda_a^D(\mathbf{F}_{\mathbf{X}^n}) + \mathbf{f}_{thm}^{n+1}, \quad \text{(SM.21)}$$

$$\mathbf{D}\cdot\mathbf{u}_p^{n+1} = 0, \quad \text{(SM.22)}$$

$$\mathbf{f}_{thm}^{n+1}(\mathbf{x_m}) = \sqrt{2\eta k_B T/L_d}(\Delta t \Delta V)^{-1/2}\mathbf{B}^{n+1}(\mathbf{x_m}), \quad \text{(SM.23)}$$

$$(\mathbf{X}_{[i]}^{n+1}-\mathbf{X}_{[i]}^n)/\Delta t = \Upsilon_a^D(\mathbf{u}_p)_i + S\ \mathrm{sgn}(t_{rev}-t^n)\left(Y_{[i]}^n, -X_{[i]}^n\right)^T, \quad \text{(SM.24)}$$

where $\tilde{p} = p - \Lambda k_B T$ is a modified pressure, Λ_a^D and Υ_a^D are the discrete versions of the structure-fluid coupling operators:

$$\left[\Lambda_a^D(\mathbf{F}_{\mathbf{X}^n})\right]_{\mathbf{m}} = \sum_i \mathbf{F}_{\mathbf{X}_{[i]}^n}(t)\,\delta_a(\mathbf{x_m}-\mathbf{X}_{[i]}^n)\Delta s_{[i]}, \quad \text{(SM.25)}$$

$$\Upsilon_a^D(\mathbf{u})_i = \sum_{\mathbf{m}} \delta_a(\mathbf{x_m}-\mathbf{X}_{[i]}^n)\mathbf{u}^{n+1}(\mathbf{x_m})\Delta x^2, \quad \text{(SM.26)}$$

where Δt is the time step, Δx is the grid size in the fluid and $\Delta s_{[i]}$ is the arclength associated with the i^{th} node on the membrane. $\mathbf{X}_{[i]}$ is the position of the i^{th} node on the membrane, with $i = 1,2,...,N$, and $\mathbf{x_m}$ is a grid point in the fluid, with $\mathbf{m} = (m^1, m^2)$ and $\mathbf{m}^l = 1,2,...,N_{\mathscr{D}}$ where $l = 1,2$. $N_{\mathscr{D}}$ is the number of the lattice points for fluid in one dimension. The term $\Delta V = (\Delta x)^2$ is the area of a unit cell, and $\mathbf{B}^{n+1}(\mathbf{x_m})$ is a spatial uncorrelated normal random tensor [9], where $\mathbf{B}_l^{n+1}(\mathbf{x_m}) \sim N(0,1)$. $\mathbf{D}$ is the standard central difference gradient operator and L is the standard 5-point discrete Laplacian. The smoothed delta functions are defined as [10–12]

$$\delta_a(x,y) = \frac{1}{a^2}\varphi\left(\frac{|x|}{a}\right)\varphi\left(\frac{|y|}{a}\right), \quad \text{(SM.27)}$$

where a is a parameter related to the support of δ_a and $\varphi(r)$, with $r \geq 0$, is defined as

$$\varphi(r) = \begin{cases} \frac{1}{8}(3-2r+\sqrt{1+4r-4r^2}) & \text{for} \quad 0 \leq \mathrm{r} \leq 1, \\ \frac{1}{8}(5-2r-\sqrt{-7+12r-4r^2}) & \text{for} \quad 1 < \mathrm{r} \leq 2, \\ 0 & \text{for} \quad 2 \leq \mathrm{r}. \end{cases} \tag{SM.28}$$

Here, we take $a = \Delta x$. The fluid system, which is subject to periodic boundary conditions, is solved using the two-dimensional Fast Fourier Transform. Although we have presented the algorithm using Euler's Method for simplicity. we actually use a stochastic RK2 method to calculate the vesicle dynamics following[8]. Because the nodes of the membrane are connected by springs, we do not discretize the inextensibility equation (3) in the main text. Instead, we take the spring constant λ_L sufficiently large so as to maintain local inextensibility to within 1% (see Sec. SM.5 in Supplementary Materials below). Finally, it remains to describe how the forces $\mathbf{F_X}$ are calculated.

Let $\Delta L = L/N$ where L is the total arclength of the membrane. Initially the nodes $\mathbf{X}_{[i]}$ are equally-distributed along the membrane with spacing ΔL. Neighboring nodes are connected by elastic springs with the spring potential being

$$E_L = \sum_{i=1}^{N} \lambda_L (\Delta s_{[i],[i+1]} - \Delta L)^2/2, \tag{SM.29}$$

where λ_L is the elastic constant, $\Delta s_{[i],[i+1]}$ is the arclength from $\mathbf{X}_{[i]}$ to $\mathbf{X}_{[i+1]}$ (details on how the arclength is calculated are given below), and $\mathbf{X}_{[N+1]} = \mathbf{X}_{[1]}$ for a closed curve. The tension between two neighboring nodes is then given by

$$\mathbf{F}_{[i],L} = \lambda_L \left(\Delta s_{i,i+1} - \Delta L\right) \left(\mathbf{X}_{[i+1]} - \mathbf{X}_{[i]}\right) / \left|\mathbf{X}_{[i+1]} - \mathbf{X}_{[i]}\right|, \tag{SM.30}$$

for $i = 1, 2, \cdots, N$, acting on the i^{th} node and pointing to the $(i+1)$ node.

The discrete elastic force density is given by

$$\mathbf{F}_{[i],\kappa} = \left(\kappa(H)_{ss,[i]} + \kappa H_{[i]}^3/2\right) \mathbf{n}_i, \quad \text{for } i = 1, 2, ..., N. \tag{SM.31}$$

The curvature $H_{[i]}$ and $(H)_{ss,[i]}$ are computed as follows. We take $\mathbf{X}_{[i]} = \left(x_{[i]}, y_{[i]}\right)$; the components are taken to be functions of the index number i as $x_{[i]} = x(i)$, $y_{[i]} = y(i)$, with $i = 1, 2, \cdots, N$. Assuming the shape of the vesicle is a smooth closed curve, we calculate dx/di and dy/di by the one-dimensional Fast Fourier Transform. Let $x_{i,[i]} = dx(i)/di$, $y_{i,[i]} = dy/di(i)$, $x_{ii,[i]} = d^2x(i)/di^2$, and $y_{ii,[i]} = d^2y(i)/di^2$. Then, the mean curvature is computed as

$$H_{[i]} = \left(x_{ii,[i]} y_{i,[i]} - x_{i,[i]} y_{ii,[i]}\right) / (x_{i,[i]}^2 + y_{i,[i]}^2)^{3/2}. \tag{SM.32}$$

The derivative of curvature H with respect to arclength s reads as

$$dH(i)/ds = H_{i,[i]}/s_{i,[i]}, \tag{SM.33}$$

where $H_{i,[i]} = dH(i)/di$ and $s_{i,[i]} = \sqrt{x_{i,[i]}^2 + y_{i,[i]}^2}$. The second derivative, H_{ss}, is then computed in a similar way. The tangent angle $\theta(i)$, $i = 1, 2, \cdots, N$, which is the angle between the tangent vector and the positive x-axis, is computed by integrating the relation $\theta_{i,[i]} = d\theta(i)/di$, using the one-dimensional Fast Fourier Transform, where

$$\theta_{i,[i]} = H_{[i]} s_{i,[i]}. \tag{SM.34}$$

Since the values of i are consecutive positive integers, $s_{i,[i]}$ is actually the local arclength associated with the i^{th} node. Thus $\Delta s_{[i]} = s_{i,[i]}$ and the arclength from $\mathbf{X}_{[i]}$ to $\mathbf{X}_{[i+1]}$ is given as

$$\Delta s_{[i],[i+1]} = \left(s_{i,[i]} + s_{i,[i+1]}\right)/2. \tag{SM.35}$$

The total force acting on the i^{th} node is the sum of the elastic and bending forces:

$$\mathbf{F}_{\mathbf{X}_{[i]}}(t) = \frac{\mathbf{F}_{[i],L} - \mathbf{F}_{[i-1],L}}{\Delta s_{[i]}} + \mathbf{F}_{[i],\kappa}, \quad \text{for } i = 1, 2, ..., N. \tag{SM.36}$$

The total area of the vesicle can then be calculated as

$$A = \sum_{i=1}^{N} \left(x_{[i]} \cos\theta_{[i]} - y_{[i]} \sin\theta_{[i]}\right) \Delta s_{[i]}. \tag{SM.37}$$

The average of the local elastic tensions, $\sigma(t)$ can be calculated as:

$$\sigma(t) = \lambda_L (L_s(t) - L)/N, \tag{SM.38}$$

where the $L_s(t) = \sum_{i=1}^{N} \Delta s_{[i]}$ is the total arclength of the discrete membrane.

SM.4 Using the immersed boundary method to simulate a fluctuating filament under tension

Since a filament is not a closed curve, we need to use a different method to calculate the bending forces. The rest of the immersed boundary method is identical to that used for the vesicle. Initially, the filament is taken to be a straight line segment equally divided into 20 sub-segments. Each sub-segment has a length of $\Delta L = 4.0 \times 10^{-7} m$ and the total length of the filament is $L = 8.0 \times 10^{-6} m$. The discrete bending energy for the filament is then defined as

$$E = \sum_{i=2}^{20} \frac{1}{2} \kappa H_{[i]}^2 \Delta L_{[i]}, \tag{SM.39}$$

where $H_{[i]}$ is the curvature at i^{th} node, which is now computed as $(\pi - \varphi_{[i]})/\Delta L_{[i]}$ for $i = 2, 3, ..., 20$, with $\Delta L_{[i]}$ the arclength associated with node i and $\varphi_{[i]}$ the angle formed by 3 successive nodes $\mathbf{X}_{[i-1]}\widehat{\mathbf{X}_{[i]}}\mathbf{X}_{[i+1]}$. The curvatures of the first and last node are set to be zero. We then use finite difference method with unequal spacing to calculate the second derivative of the curvature with respect to the arclength. The elastic force on the ends are determined by zero net force and torque conditions.

In the filament simulations, we set $\kappa = 10^{-26} J$, $\lambda_L = 10^{-4} N/m$, $\Delta t = 10^{-6} s$, and run up to 10^5 steps. We omit the first 10^3 steps and calculate the mean filament length and standard deviation from the remaining steps. For this set of parameters, we find that the standard deviation of the mean length is small, relative to the nonlinear part of the Odjik formula $< L_{NL} > = < L > - L_{Hook} = -k_B T/(2\sqrt{\kappa F_p})$ where $L_{Hook} = L_0 - F_p N_s/\lambda_L$, although it is difficult to estimate the standard deviation of the mean length because filament lengths at nearby times are correlated. Note that the bending stiffness and the spring constant here are smaller than those

used in the simulations of vesicle dynamics because of the significant computational costs associated with using the experimental parameters. For example, if one uses the experimental parameters for the vesicle, e.g., the larger bending stiffness $\kappa = 10^{-19} J$ as in [13] and spring constant $\lambda_L = 4 \times 10^4 N/m$, then $|< L_{NL} >|$ is very small (on the order of $10^{-13} m$), then many more time steps are needed to reduce the standard deviation of the mean to be a fraction of $|< L_{NL} >|$. For example, taking 10^5 steps with the experimental parameters gives the standard deviation $\sigma \approx 10^{-9} m$. Using $\sigma/\sqrt{N}$ as a rough estimate for the standard deviation of the mean length, then we would expect to require more than 10^{10} steps to reduce the standard deviation of the mean to be 10% of the mean length.

SM.5 Numerical accuracy

We demonstrate the performance of our numerical algorithm to simulate the dynamics of a vesicle in extensional flow. We take the fluid domain $\mathscr{D}$ to be a square with side length $4 \times 10^{-4} m$. The initial shape of the vesicle is an ellipse with long axis $a = 2 \times 10^{-5} m$ and short axis $b = 0.8 \times 10^{-5} m$, e.g. the aspect ratio is $a : b = 1 : 0.4$. Correspondingly, the excess arclength is $\Delta = 0.994$. The extensional flow rate is $S = 4$ (the nondimensional strain $\chi = 81$) and the bending stiffness is $\kappa = 10^{-19} J$, which is the value reported in [13] for the experimental vesicles. We set $\lambda_L = 4 \times 10^4 N/m$ to ensure that the variation of local arclength is less than 0.1% for deterministic simulations, and 0.3% for stochastic simulations. The fluids in the interior and exterior of the vesicle are assumed to have the same viscosities and densities, which are taken to be those of water at the temperature 293K (e.g., $\eta = 10^{-3} Pa\ s$ and $\rho = 10^3 kg/m^3$).

We run the simulation until the vesicle reaches an equilibrium state (up to $T = 0.1s$) using $N = 256$ interfacial nodes. We perform the simulations with time steps $\Delta t = 10^{-5} s$, $\Delta t/2$, $\Delta t/4$, and $\Delta t/8$, and check the convergence in time by measuring the vesicle area and calculating the rate of convergence r_C by

$$r_C = \log\left(|A_{\Delta t} - A_{\Delta t/2}|/|A_{\Delta t/2} - A_{\Delta t/4}|\right)/\log 2. \qquad \text{(SM.40)}$$

The results for the deterministic and stochastic immersed boundary methods are summarized in SM.Tab. 1 below and demonstrate that our numerical schemes are second-order convergent in time.

Table 1 Convergence test in time for the vesicle area ($\Delta A = |(A_s - A_{s/2}|/A$)

	Deterministic R-K 2		Stochastic R-K 2	
Time Step	ΔA	r_C	ΔA	r_C
Δt	-	-	-	
$\Delta t/2$	2.43e-8	-	3.68e-7	-
$\Delta t/4$	6.08e-9	2.002	9.18e-8	2.004
$\Delta t/8$	1.51e-9	2.008	2.34e-8	2.007

SM.6 Additional realizations of wrinkling dynamics in time-dependent extensional flow

In the main text, we presented a single realization of the stochastic dynamics of a single vesicle with excess area $\Delta = 0.994$ with two nondimensional strains $\chi = 81$ ($S = 4$) and $\chi = 323.5$ ($S = 16$). Here, we present multiple realizations for these cases to demonstrate that the results presented in the main text are characteristic of the wrinkling behavior. We also present the dynamics of a vesicle using the smaller value $\chi = 8.1$ ($S = 0.4$).

Small strain. We begin by presenting the results with $\chi = 8.1$, see SM.Fig. 1 below. The flow is reversed at time $t' = 0$. The deterministic and stochastic dynamics are shown in SM.Figs. 1[a] and [b] respectively. The corresponding experimental vesicles from [13] are shown in SM.Fig. 1[c]. The deterministic vesicles are highly symmetric and bear little resemblance to the experimental vesicles. While the stochastic vesicles are asymmetric and better resemble the two-dimensional cross-sections of the experimental vesicles, compared to the results with $\chi = 81$ and $\chi = 323.5$, the agreement with the experiments is less apparent. This is because when the strain is smaller, the relative magnitudes of the thermal fluctuations are larger than for the $\chi = 81$ and $\chi = 323.5$ cases. Consequently, three-dimensional effects in the experiments are more significant.

In SM.Fig. 1[d], the modified power spectrums $|\Delta P_m|^2$ are plotted for the deterministic (left) and stochastic (right) cases. Even though the dynamics of the deterministic and stochastic vesicles are different, the dominant wavenumbers and wavelengths are $m^* = 4$ and $\omega^* = 23.0 \mu m$ in both cases.

Moderate strain. We next present three additional realizations of the wrinkling dynamics with $\chi = 81$ in SM.Fig. 2 using the stochastic immersed boundary method. These simulations correspond to that shown in Fig. 2 (main text). The morphologies are plotted in SM.Figs. 2[a]-[c], the modified power spectrums are shown in SM.Fig. 2[d], the shapes at times t^* (see main text) are presented in SM.Fig. 2[e] and the dynamics of the elastic tensions are plotted in SM.Fig. 2[f]. As can be seen from the figure, the wrinkling dynamics of these different realizations are very similar to each other and to the case presented in Fig. 2 in the main text.

Large strain. We now present three additional realizations of the wrinkling dynamics with $\chi = 323.5$ in SM.Fig. 3. These simulations correspond to that shown in Fig. 3 in the main text. The morphologies are plotted in SM.Fig. 3[a]-[c], the modified power spectrums are shown in SM.Fig. 3[d], the shapes at times t^* (see main text) are presented in Fig. 3[e] and the dynamics of the elastic tensions are plotted in SM.Fig. 3[f]. As above, the wrinkling dynamics of these different realizations are very similar to each other and to the case presented in Fig. 3 in the main text.

SM.7 Fitting an ellipse to the vesicle and the modified power spectrum

The vesicle is fitted by an ellipse as follows. The inclination angle of the ellipse, $\Theta(t)$, is determined by the second mode of the vesicle boundary. The long axis of the ellipse is set to be the diameter of the vesicle $d = \max_{1 \le i,j \le n}(|\mathbf{X}_i \mathbf{X}_j|)$ initially and the short axis is $A/\pi d$, where A is the vesicle area. Since this might not be the best fit, we decrease d until $\int_L |\Delta P(s,t')|\, ds$ reaches its minimum, where $\Delta P(s,t)$ is the difference between the vesicle boundary and the elliptical fit.

In the main text, we calculated the modified power spectrum $|\Delta P_m|^2$ where ΔP_m are the Fourier coefficients of $\Delta P(s)$ where the Fourier transform is taken with respect to the arclength variable. Since Kantsler et al. [13], calculated the modified power spectrum

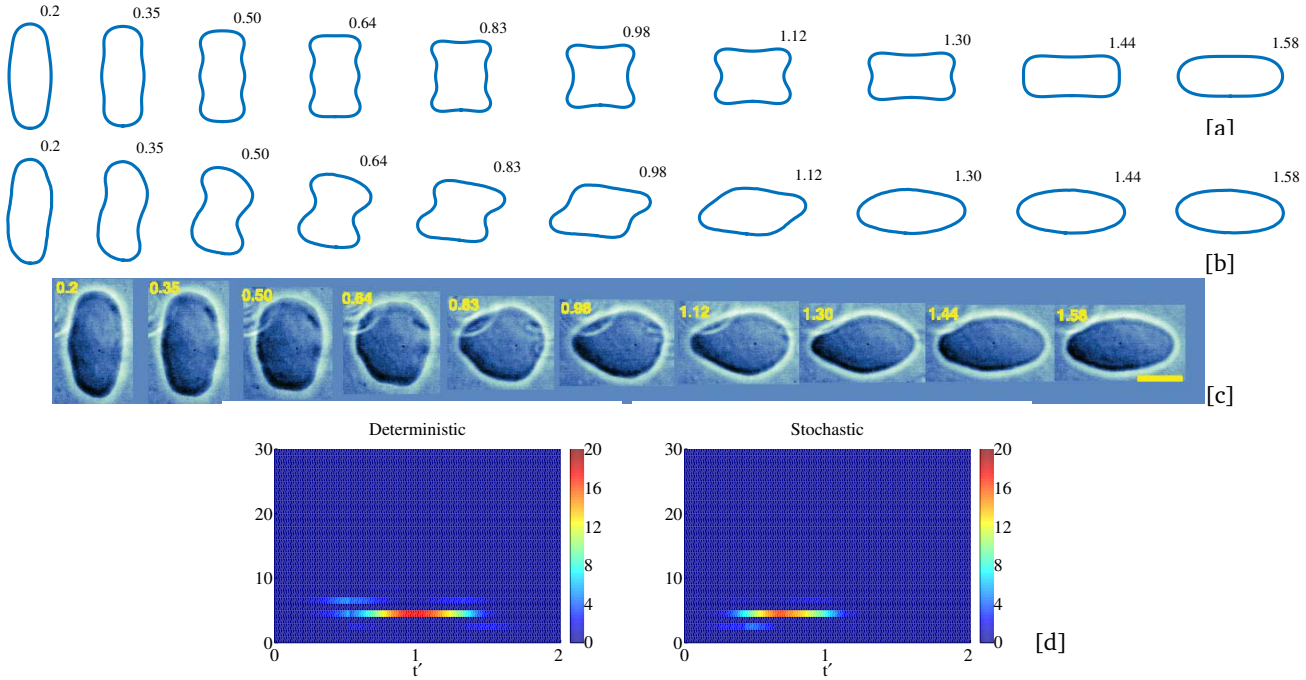

Figure 1 Dynamics of a vesicle in a time-dependent extensional flow with nondimensional strain $\chi = 8.1$ and shape parameter/excess arclength $\Delta = 0.994$. [a] Deterministic dynamics; [b] Stochastic dynamics; [c] Experimental vesicle shapes from [13] (reprinted with permission); The numbers in [a]-[c] are the nondimensional times t' at which the vesicle morphologies are shown. [d] The instantaneous modified Fourier power spectrum $|\Delta P_m|^2(t')$ (values in color). The dominant wavenumbers and wavelengths are $m^* = 4.0$ and $\omega^* = 23.0\mu m$ for each case.

with respect to the polar angle for a two-dimensional cross-section of the vesicle, instead of the arclength, we did the same. In particular, we reformulated the difference ΔP as a function of θ, the angle between $\overline{\mathbf{OX}_i}$ and positive x-axis, where $\mathbf{O}$ is the center of the vesicle (and the origin of the plane). The results are shown in SM.Fig. 4 (top) for the three realizations of the stochastic dynamics with $\chi = 81$ (presented in SM.Fig. 2). The rightmost figure on the top shows the experimental result. These figures show that the numerical simulations seem to excite higher modes than in the experiment and at slightly earlier times. A difficulty with this comparison is that Kantsler et al. did not describe the details of their elliptical fit. We found that the results could be sensitive to how the fits are actually performed. Further, in SM.Fig. 4 (bottom), we plot the the deformation $D = (L-B)/(L+B)$, where L and B are the large and small semi-axes of the elliptical approximation of the vesicle. The first three plots are the simulation results and the last plot is the corresponding plot in the experiment [13]. The simulation and experimental results are very similar and through the wrinkling and re-orientation processes the deformation decreases nearly to zero before rebounding. In the simulations, D returns to its pre-flow reversal value after re-orientation is complete. However, in the experiments, the final D is larger than the original value, indicating that two-dimensional cross section in the experiment changes size throughout the wrinkling process because of flow in the out-of-plane dimension. This can also affect the calculation of the modified power spectrum in the experiments.

SM.8 Influence of the shape parameter Δ

In Sec. 3.3 in the main text, we analyzed the effect of the initial shape parameter Δ and the flow rate on the characteristics of the wrinkling dynamics. Here, in SM.Figs. 5 and 6 we present the detailed dynamics of two cases with nondimensional flow strength $\chi = 81$. In SM.Fig. 5 the shape parameter $\Delta = 0.3079$ and in SM.Fig. 6 the shape parameter is $\Delta = 1.724$. In each figure, the deterministic dynamics is shown in [a], the stochastic dynamics in [b], the modified instantaneous Fourier spectra [c] and the shapes at time t'^* in [d]. In both cases, the deterministic dynamics are slower and the wrinkling involves higher modes than in the stochastic case. Further, the wrinkling dynamics and vesicle re-orientation occurs more rapidly when Δ is smaller since modes at lower wavenumbers are activated and there is less excess arclength.

SM.9 Budding dynamics at small strain

In the experiments by Kantsler et al. [13], it was found that the formation of buds could occur intermittently when the extensional flow direction is reversed and the strain is small. We simulated the vesicle dynamics under these conditions and present the results in SM.Fig. 7. The immersed boundary simulation results are in [a], the experimental vesicle morphologies from [13] are in [b] , and longer-time simulation results are shown in [c]. As in the experiments, the flow is reversed at time $t' = 0$. We find that like in the experiments, the simulated vesicle surface does fold inward suggesting the formation of a bud. However, bud formation in the

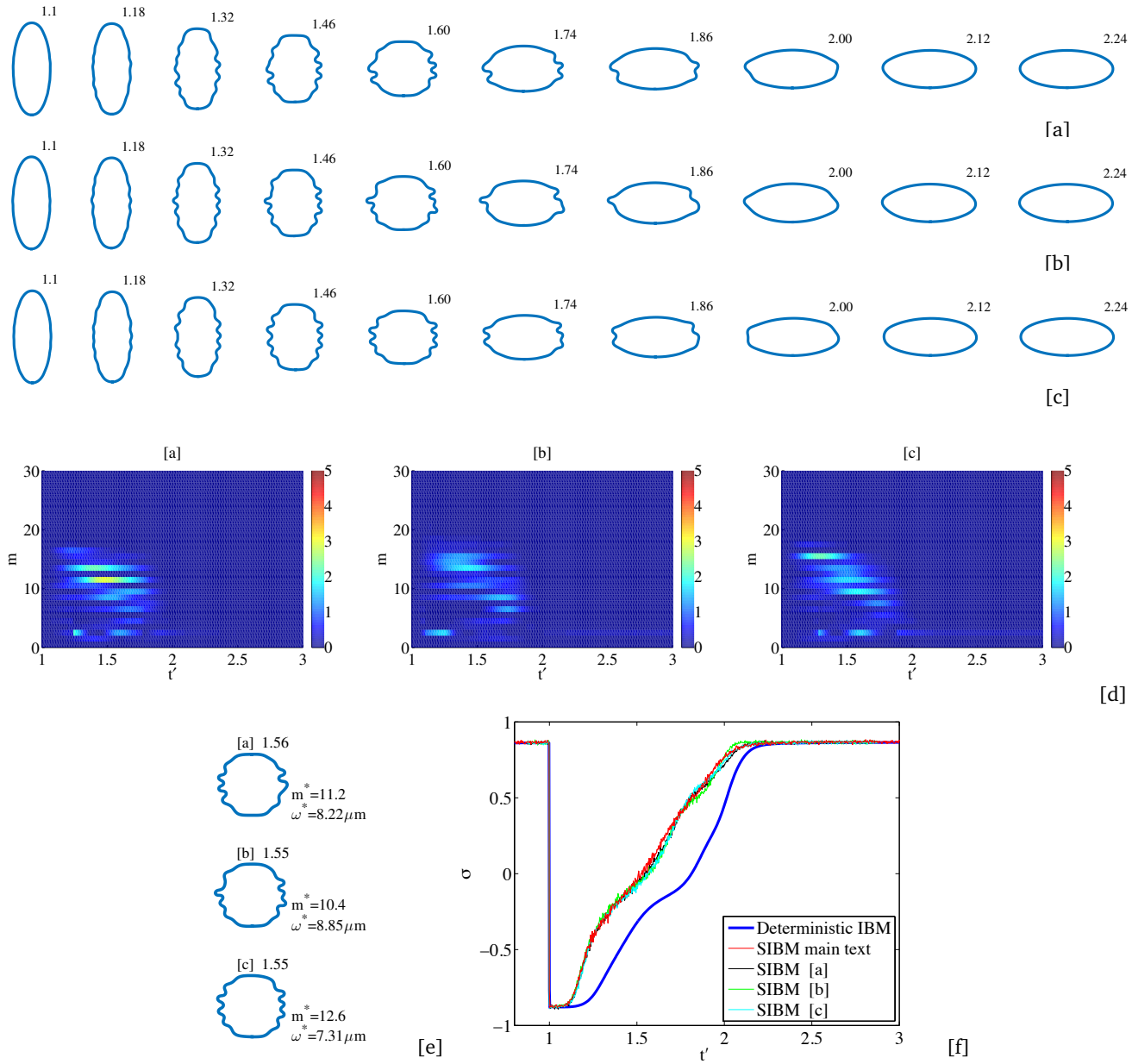

Figure 2 Three realizations of the wrinkling dynamics of a single vesicle with nondimensional strain $\chi = 81$ and excess arclength $\Delta = 0.994$. This case corresponds to Fig. 2 in the main text. [a]-[c] The vesicle morphologies; The numbers in [a]-[c] are the nondimensional times t' at which the vesicle morphologies are shown. [d] The corresponding instantaneous modified Fourier power spectra $|\Delta P_m|^2(t')$ (values in color); [e] The shapes of the vesicle at t'^* (as labeled), and the corresponding m^* and ω^*; [f] The evolution of the corresponding elastic tensions.

simulations is incomplete, likely because three dimensional effects are important. In particular, the azimuthal curvature can aid in bud formation as is evidenced in axisymmetric vesicles [14,15]. Eventually the simulated vesicle evolves to a bud-free equilibrium shape as seen in SM.Fig. 7[c].

SM.10 Wrinkling dynamics of multiple vesicles

Finally, in SM.Fig. 8, we investigate the dynamics of multiple vesicles in extensional flow. The conditions are the same as in Fig. 2 in the main text and the initial vesicles are ellipses with $\Delta = 0.994$. Each of the vesicles undergoes a transient wrinkling instability. However, in the near contact region between the vesicles, wrinkles are suppressed because inextensibility inhibits the drainage

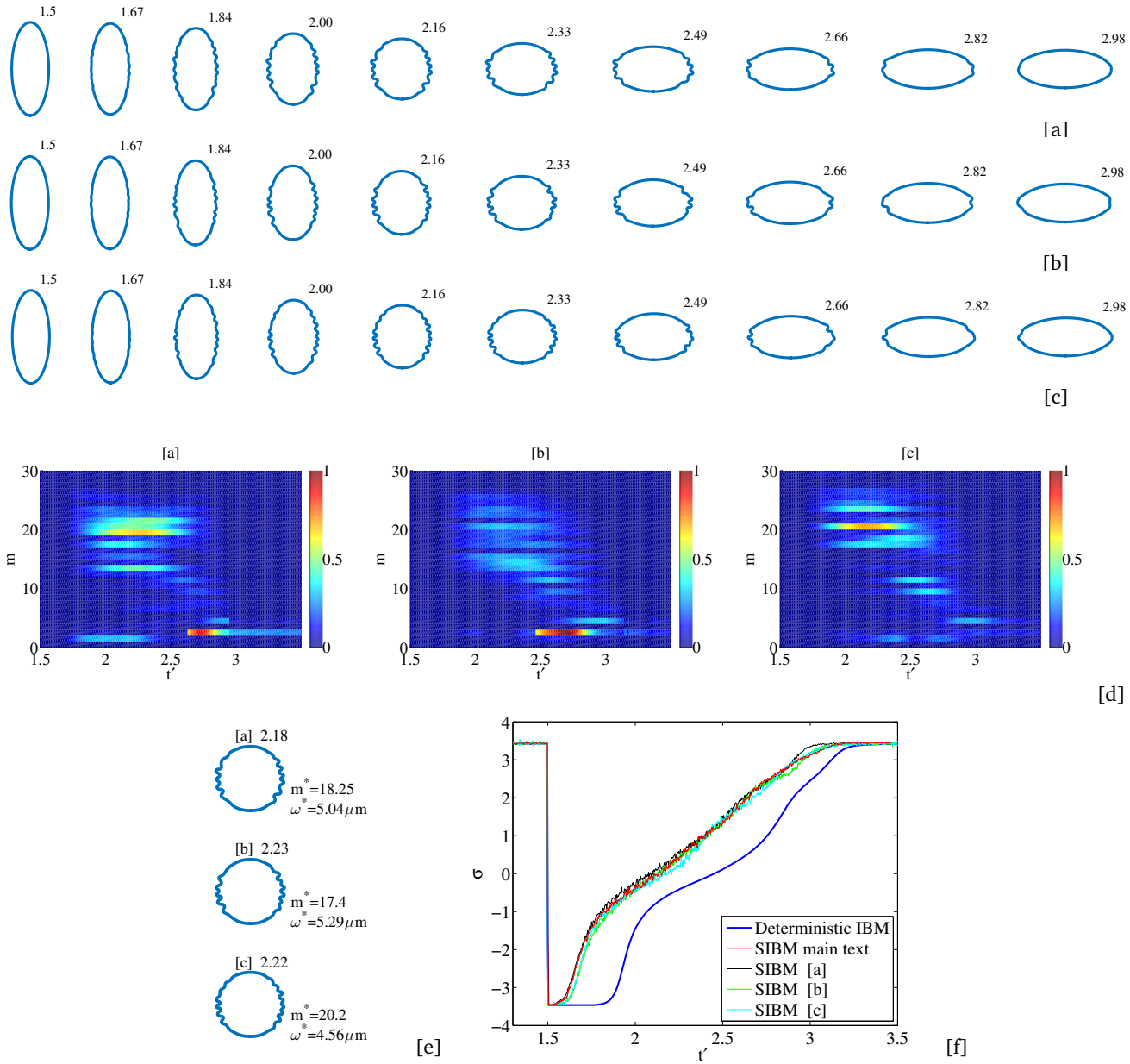

Figure 3 Three realizations of the wrinkling dynamics of a single vesicle with nondimensional strain $\chi = 323.5$ and excess arclength $\Delta = 0.994$. This case corresponds to Fig. 3 in the main text. [a] Deterministic dynamics; [b] Stochastic dynamics; [c] Experimental vesicle shapes from [13] (reprinted with permission); The numbers in [a]-[c] are the nondimensional times t' at which the vesicle morphologies are shown. [d] The instantaneous modified Fourier power spectrum $|\Delta P_m|^2(t')$ (values in color); [e] The shapes of the vesicle at t'^* (as labeled), and the corresponding m^* and ω^*; [f] The evolution of the corresponding elastic tensions.

of fluid needed to accommodate interface perturbations (e.g., see also [16]). In the simulation using two vesicles (SM.Fig. 8(left)), the dominant mode and wavelength are $m^* \approx 6.95$ and $\omega^* \approx 13\mu m$ for the vesicle on the left while for the right vesicle $m^* \approx 7.5$ and $\omega^* \approx 12.3$. Thus the wrinkling characteristics of the two vesicles are very similar to each other. The times at which the dominant modes/wavelengths occur are also very similar: $t'^*_{left} = 1.425$ for the left vesicle and $t'^*_{right} = 1.415$ for the right vesicle. Compared to the single stochastic vesicle shown in Fig. 2 [b] in the main text, the dominant mode is smaller, the wavelength is larger (recall Fig. 4 in the main text), and the time evolution is faster (recall Fig. 2 [e] in the main text). When three vesicles are simulated (SM.Fig. 8(right)), the middle vesicle is shielded from the flow

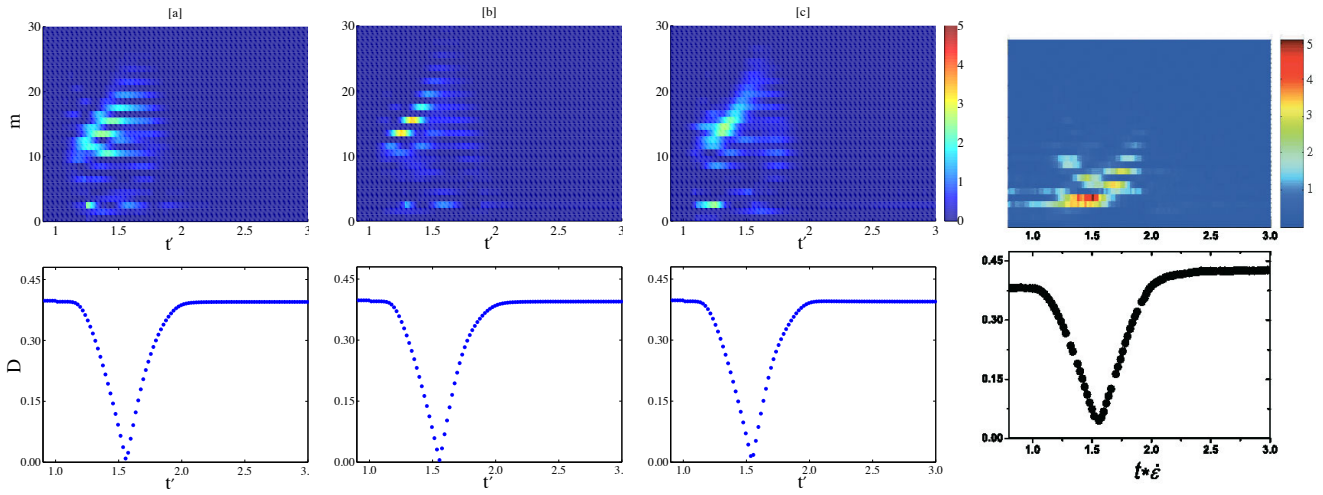

Figure 4 Top: The modified power spectrum $|\Delta P_m|^2$ where the Fourier transform is taken with respect to the polar angle θ (values in color). The nondimensional strain is $\chi = 81$ and the excess arclength $\Delta = 0.994$. This is in contrast to those presented in SM.Fig. 3 where the Fourier transform was taken with respect to arclength s. The first three plots show the simulation results from the vesicles in SM.Fig. 3 and the last plot is from the corresponding experiment in Kantsler et al.[13]. Bottom: The deformations D for the simulations (first three) and experiments (fourth).

by the outer two vesicles. Correspondingly, the dominant modes and wavelengths are different. For the leftmost vesicle, $m^* \approx 8.1$ and $\omega^* \approx 11.4\mu m$ and, for the rightmost vesicle, $m^* \approx 7.6$ and $\omega^* \approx 12.1\mu m$, which are quite similar to each other and to the corresponding values for a single, stochastic vesicle (Fig. 4 in the main text). However, the middle vesicle has $m^* \approx 5.3$ and $\omega^* \approx 17.4$, which shows that wrinkles on the middle vesicle are much more widely spaced than on the outer vesicles. The times at which the dominant modes/wavelengths occur are very similar for all three vesicles: $t'^*_{leftmost} = 1.365$, $t'^*_{middle} = 1.375$ and $t'^*_{rightmost} = 1.38$ and the wrinkling dynamics is slightly faster than the case with two vesicles.

The vesicles will not intersect if the initial positions for the vesicles are well separated and the time step Δt is small. As shown in SM.Fig. 8, we find that the wrinkling dynamics is relatively stable, that the characteristic frequencies of the wrinkles are not changed significantly by the presence of neighboring vesicles. However, nearby vesicles will partially offset thermal fluctuations since the inextensibility inhibits fluid drainage[17].

SM.11 Wrinkling dynamics in a time-dependent shear flow

We next demonstrate that wrinkling can occur in time-dependent shear flows as the flow direction is reversed. Defining an external shear flow to be $\mathbf{u}_\infty = S\mathrm{sgn}(t_{rev} - t)(y, 0)$, the nondimensional measure of flow strength can be defined using the same formula ($\chi = S\eta R^3/\kappa$) as in the extensional flow case. Note that $\mathbf{u}_\infty = \mathbf{u}_R + \mathbf{u}_E$ where $\mathbf{u}_R = \frac{S}{2}\mathrm{sgn}(t_{rev} - t)(y, -x)$ is a rotational flow and $\mathbf{u}_E = \frac{S}{2}\mathrm{sgn}(t_{rev} - t)(y, x)$ is an extensional flow– compression along $y = -x$ and extension along $y = x$. Unlike Levant et al.[7] who investigated wrinkling in the tumbling regime, we investigate wrinkling in the tank-treading regime. As in the extensional flow case, the initial ellipse is allowed to equilibrate in shear flow. Then, at time $t' = St = 1$, the flow is reversed. The vesicle morphologies, modified instantaneous Fourier spectra and elastic tensions are plotted in SM.Figs. 9[a]-[c] respectively. When the shear flow direction is reversed, the wrinkles form in the directions of compression of the underlying extensional flow $\mathbf{u}_E$, where the elastic tension is negative, and the dynamics follow a three-stage process (initiation, development, decay) as in the pure extensional flow case[18]. Here, the dominant wavenumber and wavelengths are $m^* = 7.68$ and $\omega^* = 12.0\mu m$, respectively, which are achieved at time $t'^* = 1.30$. There are apparent differences between the shear and pure extensional flow wrinkling dynamics, however. First, the dominant frequency for the wrinkling dynamics in shear flow is smaller than that in the extensional flow, as shown in SM.Fig. 9[c], because there is also a rotation of the vesicle, thus the lower even modes dominate the dynamics. Second, the wrinkling dynamics in shear flow is shorter and the average elastic tension at the equilibrium states is larger because the shear rate is two times the corresponding extensional flow rate.

References

[1] R. Kubo, *J. Math. Phys.*, 1963, **4**, 174–183.

[2] P. Kramer and A. Majda, *SIAM J. Appl. Math.*, 2003, **64**, 369–400.

[3] R. Finken, A. Lamura, U. Seifert and G. Gompper, *Euro. Phys. J. E*, 2008, **25**, 309–321.

[4] K. Liu and S. Li, *Mathematical Methods in the Applied Sciences*, 2013, 1093–1112.

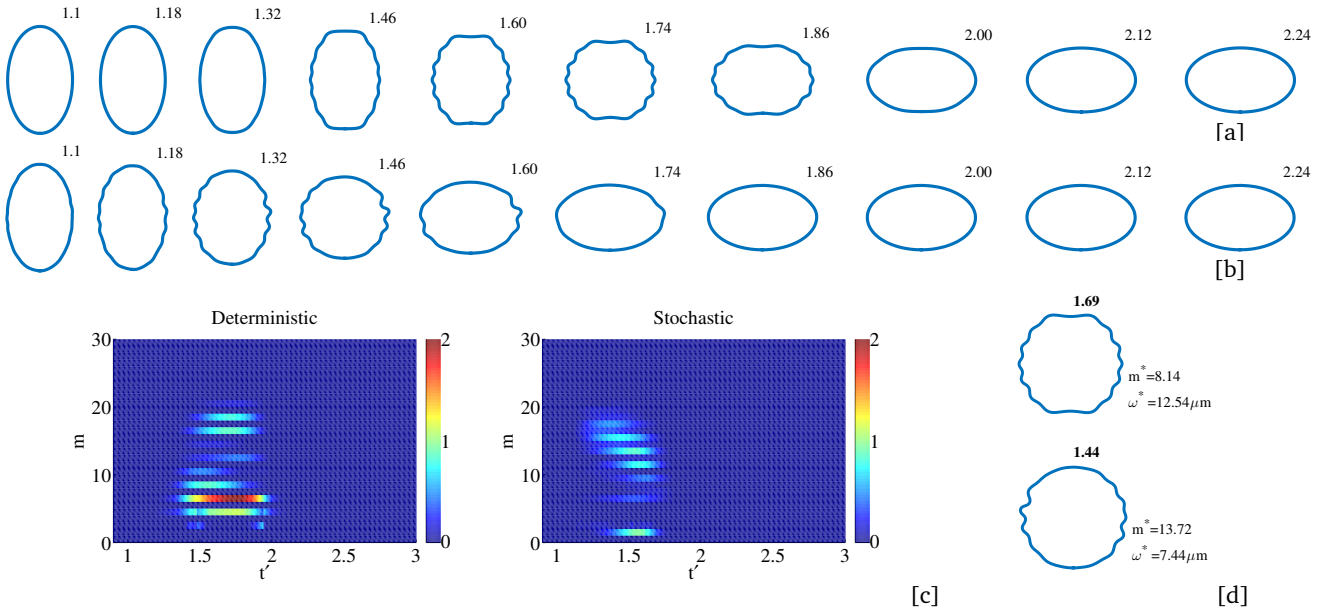

Figure 5 Wrinkling dynamics in a time-dependent extensional flow with $\chi = 81$ and excess arclength $\Delta = 0.3079$. [a]. Deterministic dynamics; [b]. Stochastic Dynamics; The numbers in [a]-[b] are the nondimensional times t' at which the vesicle morphologies are shown. [c]. The modified instantaneous Fourier spectra of the vesicle boundary (values in color); [d] The vesicle morphologies at time t'^* (as labeled), and the corresponding m^* and ω^*. Top: Deterministic; Bottom: Stochastic.

[5] K. S. Turitsyn and S. S. Vergeles, *Phys. Rev. Lett.*, 2008, **100**, 028103.

[6] U. Seifert, *Euro. Phys. J.*, 1999, **8**, 405–415.

[7] M. Levant, D. Abreu, U. Seifert and V. Steinberg, *Europhysics Letters*, 2014, **107**, 28001.

[8] A. Tocino and R. Ardanuy, *Journal of Computational and Applied Mathematics*, 2002, **138**, 219–241.

[9] F. B. Usabiaga, J. B. BelL, R. Delgado-Buscalioni, A. Donev, T. G. Fai, B. E. Griffith and C. S. Peskin, *SIAM J. Multiscale Modeling and Simulation*, 2012, **10**, 1369–1408.

[10] C. S. Peskin, *Acta Numerica*, 2002, 479–517.

[11] P. J. Atzberger, *Physica D: Nonlinear Phenomena*, 2007, **226**, 144–150.

[12] P. Atzberger, *J. Comput. Phys.*, 2007, **224**, 1255–1292.

[13] V. Kantsler, E. Segre and V. Steinberg, *Phys. Rev. Lett.*, 2007, **99**, 178102.

[14] R. Lipowsky, *Nature*, 1991, **349**, 475.

[15] *Structure and dynamics of membranes– From cells to vesicles, Vols. 1A/B*, ed. R. Lipowsky and E. Sackman, Elsevier, Amsterdam, 1995.

[16] S. Aland, S. Egerer, J. Lowengrub and A. Voigt, *J. Comput. Phys.*, 2014, **277**, 32–47.

[17] S. Aland, J. Allard and J. Lowengrub, *J. Comput. Phys.*, 2015, **309**, 112–128.

[18] K. Liu, *Dynamics of vesicles in viscous fluid*, Ph.D. thesis. Illinois Institute of Technology, Chicago, 2014.

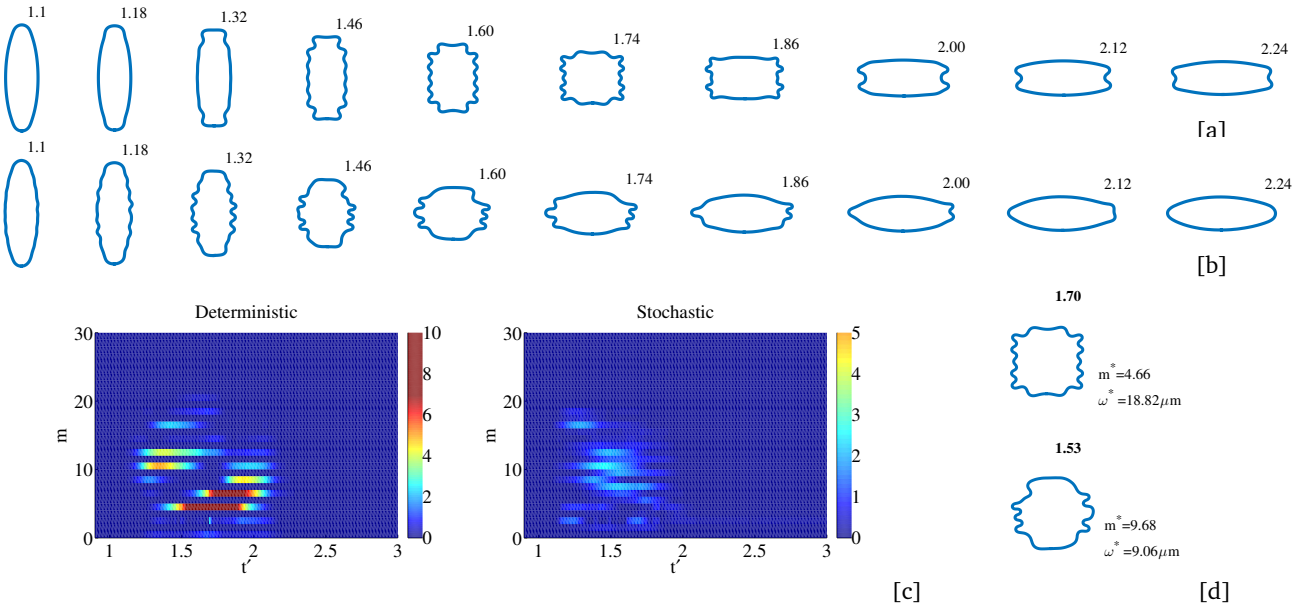

Figure 6 Wrinkling dynamics in a time-dependent extensional flow with $\chi = 81$ and excess arclength $\Delta = 1.724$. [a]. Deterministic dynamics; [b]. Stochastic Dynamics; The numbers in [a]-[b] are the nondimensional times t' at which the vesicle morphologies are shown. [c]. The modified instantaneous Fourier spectra of the vesicle (values in color); [d] The vesicle morphologies at time t'^{*} (as labeled), and the corresponding m^{*} and ω^{*}. Top: Deterministic; Bottom: Stochastic.

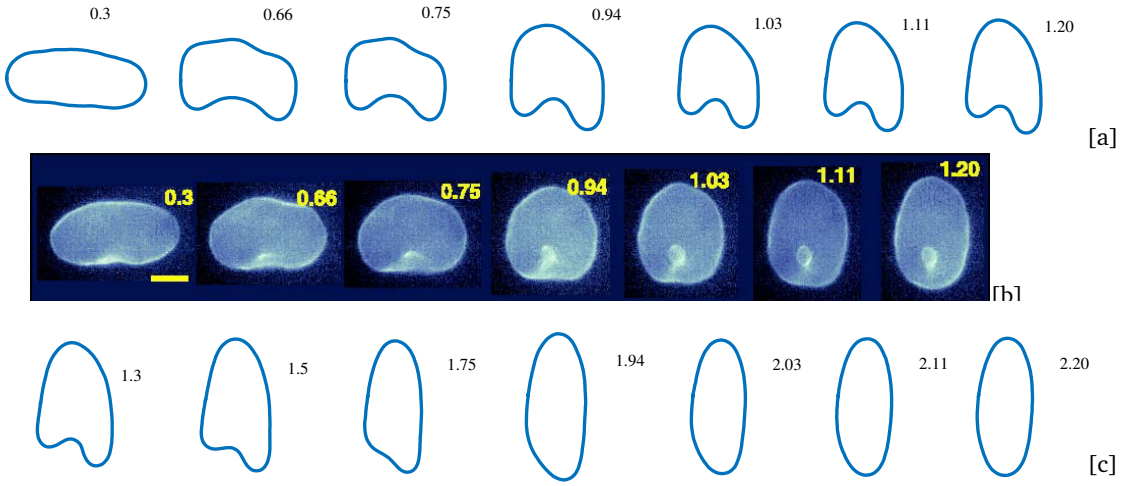

Figure 7 Budding dynamics in a time-dependent extensional flow with $\chi = 6.8$ and shape parameter $\Delta = 0.994$. [a]. Immersed boundary simulation; [b] experimental dynamics from [13] (reprinted with permission); [c] Immersed boundary simulation at longer times. The numbers in [a]-[c] are the nondimensional times t' at which the vesicle morphologies are shown.

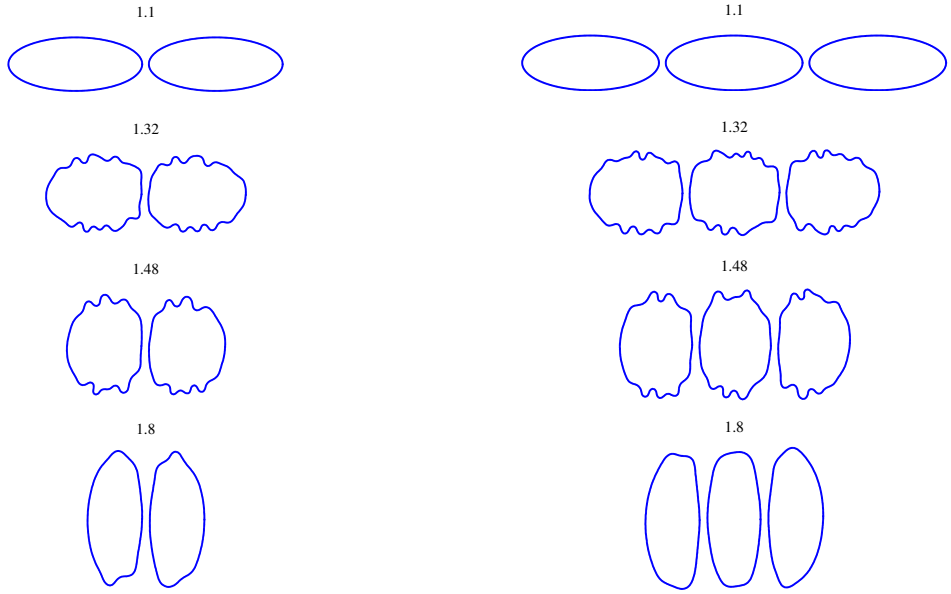

Figure 8 The wrinkling dynamics of multiple vesicles using the stochastic immersed boundary method. The vesicles are initially ellipses with $\Delta = 0.994$ and the nondimensional strain is $\chi = 81$. The flow is abruptly started at $t' = 1$. Left: Two vesicles; Right: Three vesicles. Each of the vesicles undergoes a wrinkling instability although the wrinkling characteristics depend on vesicle location (see text).The numbers are the nondimensional times t' at which the vesicle morphologies are shown.

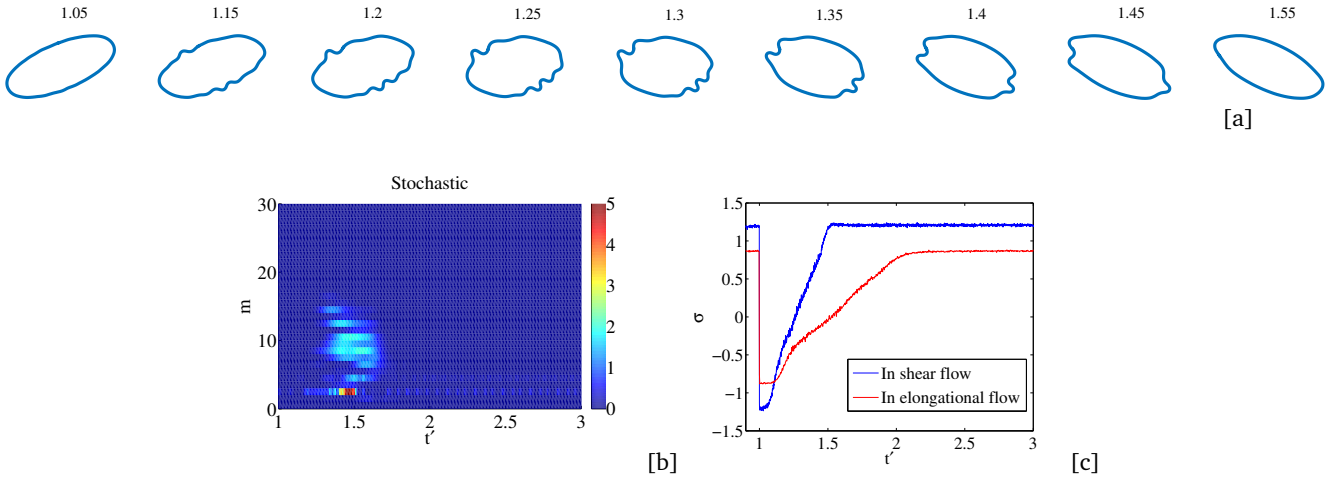

Figure 9 Wrinkling dynamics in a time-dependent shear flow with nondimensional shear rate $\chi = 162$ and excess arclength $\Delta = 0.994$. [a]. Vesicle morphologies. The numbers are the nondimensional times t' at which the vesicle morphologies are shown. [b]. The modified instantaneous Fourier spectra (values in color); [c]. The elastic tension dynamics for shear flow (blue) and pure extensional flow (red, with $\chi = 81$).